Simulation of material failure behavior under different loading rates using molecular dynamics

Kunhwi Kim[†], Jihoon Lim[‡], Juwhan Kim[‡†] and Yun Mook Lim[‡‡]

School of Civil and Environmental Engineering, College of Engineering, Yonsei University 134, Sinchon-dong, Seodaemun-gu, Seoul 120-749, Korea

Abstract. Material failure behavior is generally dependent on loading rate. Especially in brittle and quasi-brittle materials, rate dependent material behavior can be significant. Empirical formulations are often used to predict the rate dependency, but such methods depend on extensive experimental works and are limited by practical constraints of physical testing. Numerical simulation can be an effective means for extracting knowledge about rate dependent behavior and for complementing the results obtained by testing. In this paper, the failure behavior of a brittle material under different loading rates is simulated by molecular dynamics analysis. A notched specimen is modeled by sub-million particles with a normalization scheme. Lennard–Jones potential is used to describe the interparticle force. Numerical simulations are performed with six different loading rates in a direct tensile test, where the loading velocity is normalized to the ratio of the pseudo-sonic speed. As a consequence, dynamic features are achieved from the numerical experiments. Remarkable failure characteristics, such as crack surface interaction/crack arrest, branching, and void nucleation, vary in case of the six loading cases. These characteristics are interpreted by the energy concept approach. This study provides insight into the change in dynamic failure mechanism under different loading rates.

Keywords: dynamic fracture mechanics; rate dependency; molecular dynamics; energy concept approach.

1. Introduction

Every material exhibits various failure behaviors under different strain or loading rates, the so-called rate dependency. In the case of brittle or quasi-brittle materials such as concrete under impact loading, the effect of loading rate can be more significant (John and Shah 1990). However, the failure behavior induced by dynamic loading is not fully understood, so rate dependency has often been neglected in classical fracture mechanics (Anderson 1995). Most experiments suffer from constraints in handling the equipment for controlling the dynamic fracture. The difficulty of sustaining constant strain rate and the presence of wave motion in the specimen often necessitate an indirect experimental method such as a Hopkinson bar (Lok *et al.* 2003). Moreover, instability of

---

† Ph.D. Candidate
‡ M.S., Research Engineer
‡† Ph.D., Research Fellow
‡‡ Ph.D., Associate Professor, Corresponding author, E-mail: yunmook@yonsei.ac.kr

dynamic fracture has induced the following unsettled phenomena in the case of brittle materials such as polymethyl methacrylate (PMMA), Homalite-100, and glasses (Fineberg and Marder 1999).

• Disagreement between theoretical and experimental crack propagation speeds: It is reported that a crack can grow as fast as the sound speed on a solid surface, known as the Rayleigh wave speed theoretically (Freund 1998), but the observed speeds are only approximately 40% to 70% of this speed (Fineberg and Marder 1999, Kobayashi *et al.* 1974). Recently, Abraham has elucidated that the idealized crack propagation speed was transonic in the MD simulation of his specimens (Abraham 2001a). However, the understanding of the crack propagation speed is still not complete, which is attributed to the dynamic crack instability.

• Generation of heat energy during crack growth: The strain energy stored in the specimen is released when the crack moves. Some of the energy is also converted into heat, sound, vibration, etc., and in most cases the strain energy is converted to heat energy (Döll 1973, Zimmerman *et al.* 1984). The generation of heat is observed around the crack path in particular, so it seems to be closely correlated to the crack growth. However, the mechanism of heat generation and its relationship to the fracture energy have not been clarified yet.

• Roughness of the crack surface: The experimental research concerning crack roughness is usually accompanied by observations of the crack surface using optical or electronic microscopes, but the results are strongly dependent on the accuracy of the devices. It has been known that the shape of crack surface is not related to loading conditions and initial specimen configurations, but the primary factors of crack roughness still remain to be found.

• Multiple crack fronts and crack branching: Ravi-chandar and Knauss (1984) performed an experimental research with a brittle material, where microscopic voids were generated during the cracking process, which then evolved into multiple crack fronts. This phenomenon is generally caused by the highly concentrated stress at the crack tip (Broberg 1979). Furthermore, a crack can branch into two or more cracks if the multiple crack fronts develop occasionally. Eshelby (1971) has stated that the crack branching can occur when the fracture energy is input into the system such that there is adequate growth of multiple cracks. Unfortunately, the relationship between the fracture energy and the crack propagation speed is not backed up by this assertion, so further research concerning crack branching is necessary.

Meanwhile, well-established methods that consider the continuum mechanics approach have limitations with regard to the dynamic failure behavior (Krivtsov and Wiercigroch 2001). The conventional analysis methods such as the finite element (FE) method and the boundary element (BE) method are limited by their macroscopic view of physical phenomena and various assumptions adopted in the constitutive laws. However, in the last few decades, a microscopic analysis method, namely, molecular dynamics (MD), has been introduced to a large variety of problems in mechanics and physics. The MD enables a direct and detailed analysis under highly dynamic conditions. Unlike the conventional methods, the MD does not require pre-determined properties, but instead these parameters can be found from the numerical experiments. The domain is modeled by a large number of particles and the material behavior is represented by the motion of the particles. The trajectories of particles are formulated by integrating over time the classical equations of motion, where the inter-particle forces are derived from the potential energy between particles. As computer resources and implementation techniques have undergone advancements, the method can be applied to dynamic fracture mechanics to solve problems of the extent of mesoscopic level for the simulation of dynamic features such as inter-sonic crack propagation (Gao *et al.* 2001),

polycrystalline effects (Krivtsov and Wiercigroch 2001), and dynamic instability affected by hyperelasticity (Buehler *et al.* 2003, Buehler and Gao 2006).

This study aims to simulate the change of failure features under various loading rates and give insight into the dynamic failure mechanism. Similar studies have been performed to simulate the fracture behavior at high strain or loading rates. However, the research conducted by Wagner *et al.* (1992) was limited to rather small size of specimens (about 16000 particles) with periodic boundaries that could not explicitly represent the actual boundaries. Whereas Zhou *et al.* (1996) applied absorbing boundaries in the specimen, but this likely did not consider the reflected waves from the boundaries. In this study, numerical experiments of a direct tensile test are simulated for a brittle material (a Lennard–Jones (LJ) potential-based material) with a notch and explicit boundary conditions under different loading rates. The rate dependent features obtained from the results can provide qualitative understanding of the dynamic failure mechanism.

2. Methodology of the molecular dynamics simulation

2.1 The motion of particles

The MD method requires the definition of a potential function by which the particles interact in the simulation. Various kinds of potential functions may be defined for many types of the molecules and for many levels of physical accuracy. In this research, the Lennard–Jones (LJ) potential function is used, which is a description of the distance between two particles.

The formulation to calculate the trajectories of particles is simply from equations of motion. First, the acceleration of a particle is derived from Newton's second law as

$$a_i = \frac{1}{m}\sum_{j \neq i} F_{ij} \qquad (1)$$

where F_{ij} is the inter-particle force from a neighbor particle and m is the particle mass. Next, by integrating the acceleration in time, the velocity and the position of a particle are calculated. In this research, Beeman's algorithm is used to integrate the acceleration numerically with the time increment Δt. However, at the first time step, the Beeman's algorithm cannot be applied because it requires the acceleration terms in past two steps, so velocity Verlet algorithm substitutes for it.

In the MD simulation, the initial position and velocity of particles are important for describing the material configuration. Krivtsov (2003) used the random position distribution of particles, but a part of particles escaped from the domain during the simulations. Thus, he replenished particles with the Mie Potential until the specimen attained the target density. However, the procedure is complicated and time-consuming to follow this configuration, so an alternative to set the initial distribution is considered in this research. In the view of microscopic thermodynamics, the temperature of a system T can be calculated from

$$\frac{1}{2}m\bar{v}^2 = \frac{3}{2}k_b T \qquad (2)$$

where $\bar{v}^2$ is a mean square of the velocity distribution and k_b is the Boltzmann constant. A general physical material shows various phases with the change in temperature, so the material phase can be
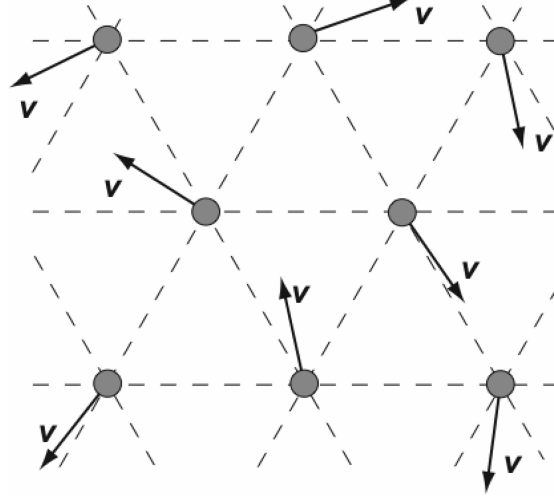
Fig. 1 Particle layout with initial velocity in the equilibrating stage

controlled by $\bar{v}^2$ in the simulation. In the equilibrating stage before the main analysis, all particles are distributed on the triangular grid sharing the same scalar of velocity, but the direction of the velocity is randomized as shown in Fig. 1. Then, the system goes through the pre-analysis until the total potential energy is stabilized. During the equilibration, the uniform velocity distribution changes to the Maxwell–Boltzmann distribution, whereas the average kinetic energy—the adiabatic analysis—is retained. By doing so, the system is believed to describe the target material well enough.

2.2 Normalized governing equations

As noted in the Introduction, the MD method is a microscopic approach. On this account, billions to trillions of particles should be modeled to simulate the macroscopic problems using the MD method on actual scale. The massive computations can be reduced using normalizing units in the governing equations.

From Eq. (1), the acceleration a_i of an LJ potential-based particle can be rewritten as

$$a_i = \sum_{j \neq i} \frac{24\varepsilon}{m}\left(\frac{2\sigma^{12}}{r_{ij}^{13}} - \frac{\sigma^6}{r_{ij}^7} \right) \tag{3}$$

Here, two specific parameters for the LJ potential function are introduced; one is the atomic distance, named as the equilibrium separation length $r_0 = 2^{1/6}\sigma$ where the inter-particle force becomes zero, and the other is the force constant k given as

$$k = \frac{dF_{ij}}{dr_{ij}}(r_0) = \frac{72\varepsilon}{r_0^2} \tag{4}$$

With the terms r_0 and k, Eq. (3) can be modified as

$$a_i = \sum_{j \neq i} \frac{r_0 k}{6m}\left[\left(\frac{r_0}{r_{ij}}\right)^{13} - \left(\frac{r_0}{r_{ij}}\right)^7 \right] \tag{5}$$

Then with the normalized term of distance $\eta_{ij} = r_{ij}/r_0$ and the natural frequency $\omega = \sqrt{k/m}$, Eq. (5) is simplified as

$$a_i = \sum_{j \neq i} \frac{r_0 \omega^2}{6} \left[\left(\frac{1}{\eta_{ij}} \right)^{13} - \left(\frac{1}{\eta_{ij}} \right)^7 \right] \tag{6}$$

Suppose the wavelength λ is equivalent to r_0, $v_s = r_0 \omega$ can be regarded as the pseudo-sonic speed. With this term, Eq. (6) will be expressed as

$$a_i = \sum_{j \neq i} \frac{\omega v_s}{6} \left[\left(\frac{1}{\eta_{ij}} \right)^{13} - \left(\frac{1}{\eta_{ij}} \right)^7 \right] \tag{7}$$

Next, the Beeman's algorithm is modified to give the normalized formulation. The equations for calculating the position and the velocity are divided by r_0 and v_s, respectively

$$\frac{r_i(t+\Delta t)}{r_0} = \frac{r_i(t)}{r_0} + \frac{v_i(t)}{v_s}(\omega \Delta t) + \frac{2}{3}\frac{a_i(t)}{\omega v_s}(\omega \Delta t)^2 - \frac{1}{6}\frac{a_i(t-\Delta t)}{\omega v_s}(\omega \Delta t)^2 \tag{8}$$

$$\frac{v_i(t+\Delta t)}{v_s} = \frac{v_i(t)}{v_s} + \frac{1}{3}\frac{a_i(t+\Delta t)}{\omega v_s}(\omega \Delta t) + \frac{5}{6}\frac{a_i(t)}{\omega v_s}(\omega \Delta t) - \frac{1}{6}\frac{a_i(t-\Delta t)}{\omega v_s}(\omega \Delta t) \tag{9}$$

Note that the term v_i/v_s is called pseudo-Mach number μ_i. Also, from the above normalization process, the terms r_i/r_0 and $a_i/\omega v_s$ are the normalized distance and acceleration, respectively, symbolized as η_i and α_i. With these terms, Eqs. (8) and (9) are rewritten in a simple form as follows

$$\eta_i(t+\Delta t) = \eta_i(t) + \mu_i(t)(\omega \Delta t) + \frac{2}{3}\alpha_i(t)(\omega \Delta t)^2 - \frac{1}{6}\alpha_i(t-\Delta t)(\omega \Delta t)^2 \tag{10}$$

$$\mu_i(t+\Delta t) = \mu_i(t) + \frac{1}{3}\alpha_i(t+\Delta t)(\omega \Delta t) + \frac{5}{6}\alpha_i(t)(\omega \Delta t) - \frac{1}{6}\alpha_i(t-\Delta t)(\omega \Delta t) \tag{11}$$

where $\omega \Delta t$ is the normalized time increment. For the stability of the algorithm in the simulation, $\omega \Delta t$ should be less than $\pi/2$ according to the Courant condition. The value of $\omega \Delta t$ is selected in the range of $0.025\pi/2$ to $0.05\pi/2$ in this study.

Using the above normalization scheme, the computation is considerably advantageous for simplifying variables and coefficients during the simulation. Moreover, the feasibility to the macro-level engineering field can be expected with the results from this normalized MD simulation in that the self-similarity has been found up to the mesoscopic level in other previous researches (Robertson *et al.* 1997).

3. Composition of specimens

The numerical experiments are simulated with a two-dimensional plate model, which has the following advantages (Abraham 2001b): First, a two-dimensional simulation takes less operation count than a three-dimensional case with the same number of particles. Second, the triangular grid shows elastically isotropic behaviors in a small deformation. Third, the LJ potential-based particles in the two-dimensional grid behave as a brittle material. For that reason, the two-dimensional model
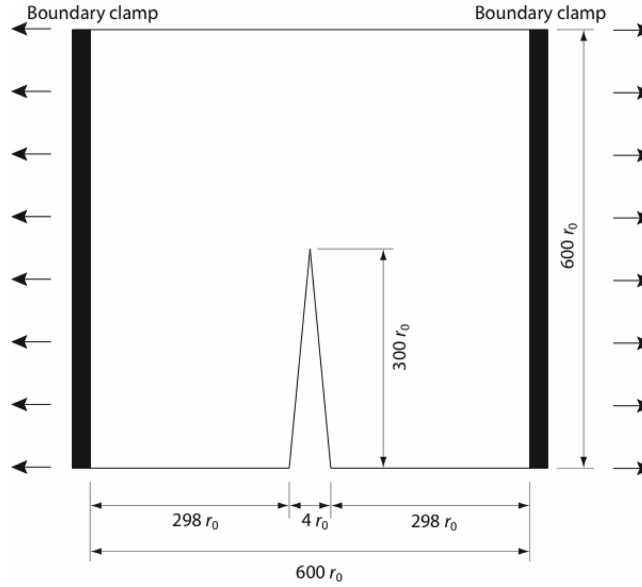
Fig. 2 Schematic drawing of the test specimen

is regarded to be quite competent for simulating the fracture of the target material (Abraham 2001b) although the three-dimensional simulation has been used in previous studies (Zhou *et al.* 1997).

The material specimen is modeled with particles placed at the triangular grid with spacing of r_0 as shown in Fig. 2. The specimen has a square shape of $600r_0$ by $600r_0$, and the total number of particles in the specimen is approximately 0.41 million. In the center of the specimen, a notch extends to a half of the height from the bottom. Extra particles are padded at both left and right boundaries to represent loading clamps. Ten layers of particles on each side are modeled, and the boundary layers are moved according to the designed loading rates. The boundary particles physically interact with the specimen particles, so the reflective stress waves can be generated from the boundaries during the simulation.

The average velocity of particles is calculated at the melting point and normalized in terms of v_s. It turns out that the normalized system depends only on v_s of the target material, and once the value is known, the average Mach number at melting point is an invariant among different materials. Hence, the model yields the changeable scales where the parameters are not confined to a specific material size. The velocity of particle is set to the target value in the randomized direction so that the specimen is put under pre-analysis (i.e., the equilibrating stage) where the boundary clamps are at rest. In the process, the velocity distribution equilibrates to the Maxwell–Boltzmann distribution and the particles move to the optimal position for the potential equilibrium.

The specimens are simulated using the displacement control method to the tensile direction for Mode I fracture, where the boundary clamps moves with various loading rates (0.03%, 0.05%, 0.1%, 0.3%, 0.5%, and 1.0% of v_s). Every 20 steps during the analysis, normalized positions of particles, along with velocities expressed in the Mach number are recorded.

In the post-processing stage, positions of particles are tessellated using the Delaunay triangulation, and then the Voronoi cells are generated from the triangulation. The area occupied by each Voronoi cell is calculated, and then a number density corresponding to the area is given to each particle. For

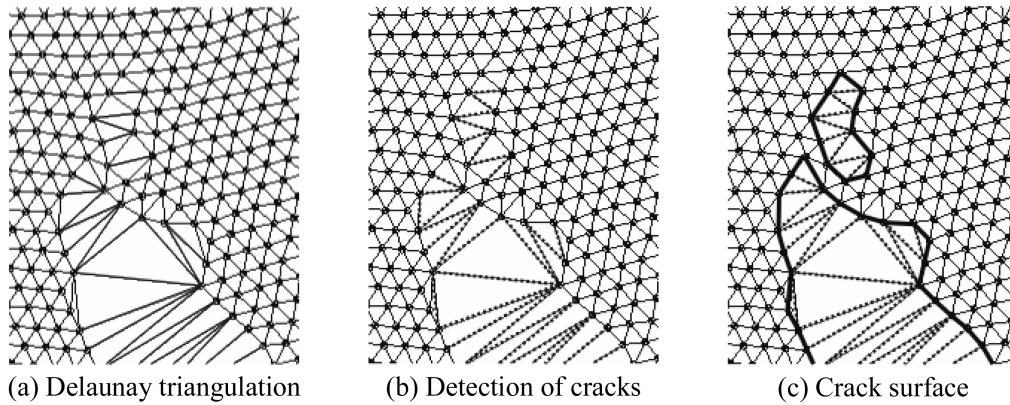(a) Delaunay triangulation   (b) Detection of cracks   (c) Crack surface

Fig. 3 Construction of crack surface with cutoff radius $2r_0$

visualization, the density diagram is projected onto a graphical view port with density value byte scaled to help identify the features. The velocity undergoes similar treatment in which it is converted to a fraction of the melting point. The value sets are then triangulated, interpolated, and projected. Fig. 3 shows the process for the detection of the crack in the specimen. From the Delaunay triangulation (Fig. 3(a)), the selective triangles are identified, in which at least one of the sides is longer than $2r_0$ (dotted lines in Fig. 3(b)), then the crack surface is constructed by connecting the other sides of the triangles (bold lines in Fig. 3(c)). Here, $2r_0$ is regarded as a cutoff radius where the inter-particle force is nearly zero. The length around these contours, the crack surface length, will be an indicator of crack roughness.

4. Results and discussion

Dynamic failure features result from the direct tensile test on a brittle material specimen with a notch. With six different loading rates, the characteristic phenomena are found to vary, i.e., rate dependent results. As the loading rate increases, the fracture behavior tends to be ductile and unstable characteristics occur regardless of the fast crack propagation speed.

Fig. 4 shows the arrangement of the density snapshots where the loading rate varies in row and each column depicts the same global strain (0.448%, 0.896%, 1.344%, 1.792%, and 2.24%). Since the local strain and strain rate vary inside the specimen, the global strain and loading rate are used as comparison parameters. Crack propagation is noticeably retarded at higher loading rates. While the specimen of the case at 0.03% of v_s is completely separated to two pieces in the last column, cases 0.05% and 0.1% show approximately 75%, case 0.3% shows approximately 50%, case 0.5% shows approximately 25%, and case 1.0% shows approximately 10% of crack growth from the initial notch tip. Note that Fig. 4 arranges global strain-based snapshots in columns instead of time-based snapshots. This arrangement visualizes the crack length versus the global strain relationship similar to the conventional stress-strain response. Also note that the actual time to achieve the same global strain decreases as the loading rate increases.

The dark regions in Fig. 4 represent the lower density zone. Lower density may indicate the softening behavior in that the distance between particles tends to increase. This softening zone appears more widely around the crack tip in higher loading-rate cases. In particular, in the cases of
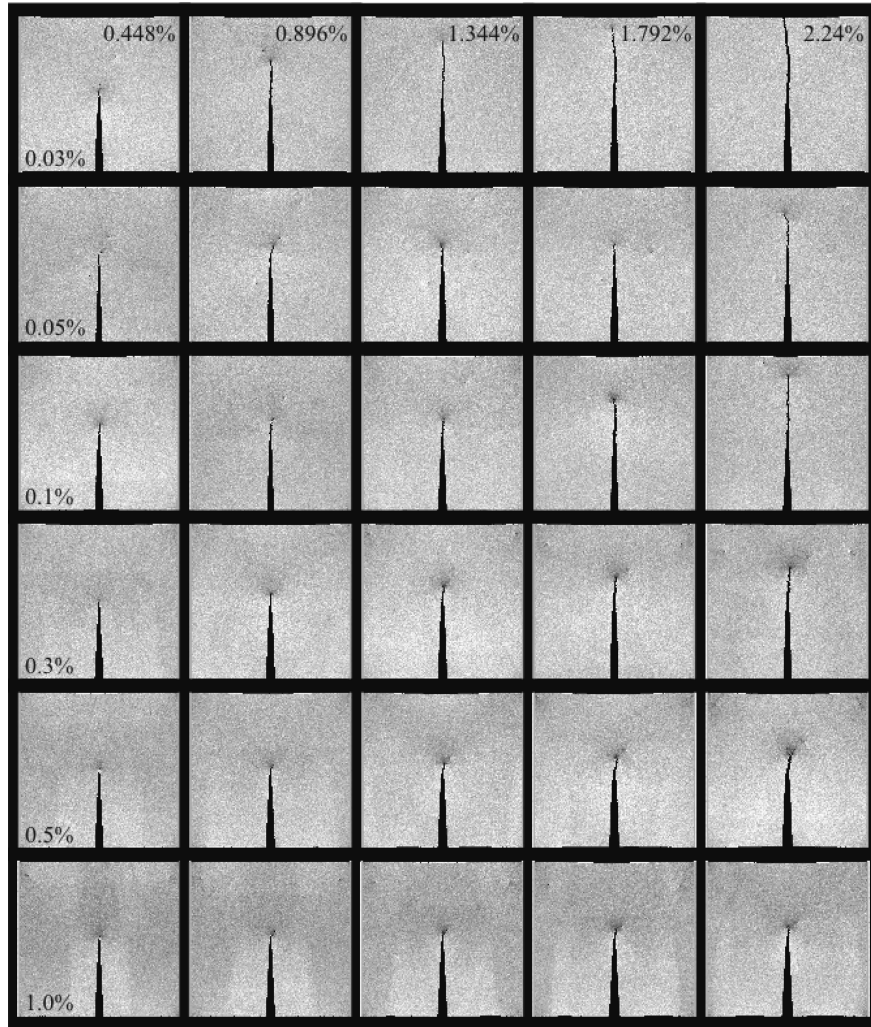
Fig. 4 Crack propagation profile represented in the density snapshots

0.5% and 1.0% of v_s, the zone appears ahead of the crack tip like the plastic zone protrudes due to the increase of strain energy (Buehler and Gao 2006). This may be interpreted as that a surplus energy is partially accumulated around the crack tip, and more spacious softening zone appears at higher loading rates. The expansion of the plastic zone will be clearly demonstrated later in the potential energy snapshots (Fig. 9(b)).

The lower density zone can affect the direction of the crack growth (Gao *et al.* 2001). It may be also related to the crack surface roughness. Fig. 5(a) shows the density diagram near separation of the specimen to help understand the roughness of the crack surface. Note that each density diagram is at a different global strain, in contrast to Fig. 4. In addition, the shockwave pattern from the crack tip is captured, which becomes vivid as the loading rate increases. Geometrically, the roughness of crack leads to an increase in the crack surface length. At the complete separation of the specimen, the crack surface length can be calculated using the Delaunay triangulation of particles as referred to in the previous section. Fig. 5(b) shows the curve indicating the relationship between the crack

(a) Density diagrams of the separated specimens

(b) Crack surface length corresponding to different loading rates
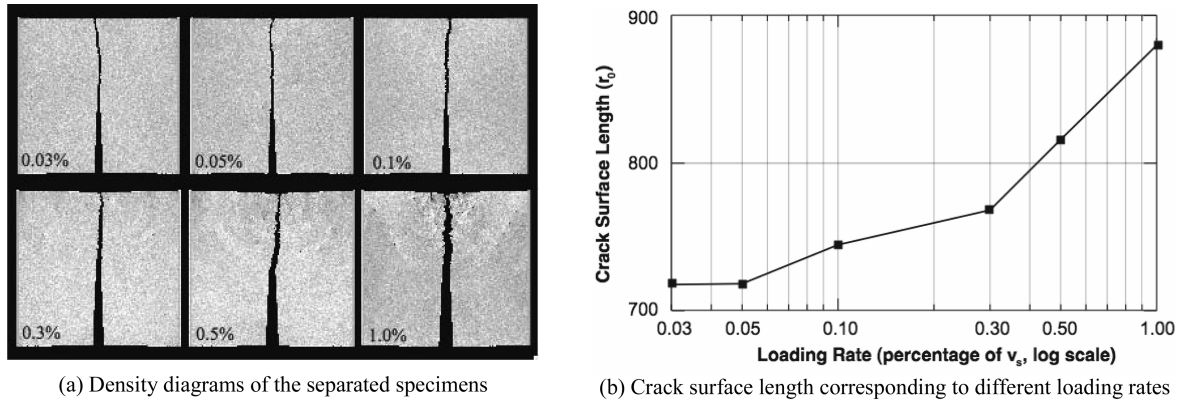
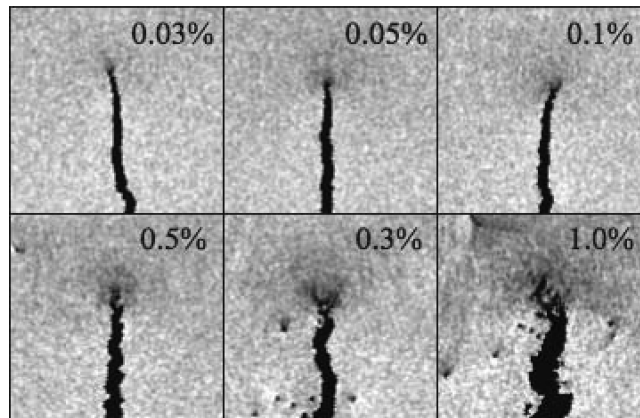Fig. 5 Crack roughness at the complete separation of the specimen

Fig. 6 Magnified density diagram around the crack tip

surface length and the loading rates. As can be seen in Fig. 5, the crack surface length increases as the loading rate increases, i.e. the cracks become rougher. It can be pointed out that more energy is required for the growth of the crack at higher loading rates.

The magnified density diagrams around the crack tips are arranged as in Fig. 6. In higher loading-rate cases (0.5% and 1.0% of v_s), many black holes appear near crack surface, the so-called void nucleation. Also, the crack tip is separated into multiple crack fronts and the crack width is larger in higher loading-rate cases. Though the void nucleation also occurs at lower loading rates, it is lethargic and cannot develop to the multiple crack fronts. It is reported that the multiple crack fronts or the crack branching can be generated by connecting the voids to the main crack at higher loading rates, while the voids appear ahead of the crack and lead the main crack growth at lower loading rates (Ravi-chandar and Knauss 1984).

According to the features above, it is judged that the increase of the loading rate brings about the ductile failure of the target material. This judgment seems to be against to the general rate dependent tendency to be brittle under higher loading rates. However, an experimental research, conducted by Kozhushko and Sinani (2005), elucidates the reversible characteristics in the exceedingly high loading velocity. In that research, the penetration test was performed with several brittle solids over a wide range of indentation (or impact) velocities (from 10^{-4} to 10^3 m/s) and they

compared the ratio of the indentation resistance to the material hardness, an indicator of the material toughness. The degraded resistance ratio (i.e., ductile-brittle transition), due to the increase of the loading velocity at the level of indentation, recovers to cause the reverse brittle-ductile transition as the loading velocity keeps increasing to level of impact, the so-called hypervelocity impact. The actual strain rate for the present simulation is around 10^6 to 10^7, so the loading velocity might be in the range of the hypervelocity impact.

Fig. 7 shows the number of debonded link variations as the time step increases at different

(a) 0.03%

(b) 0.05%

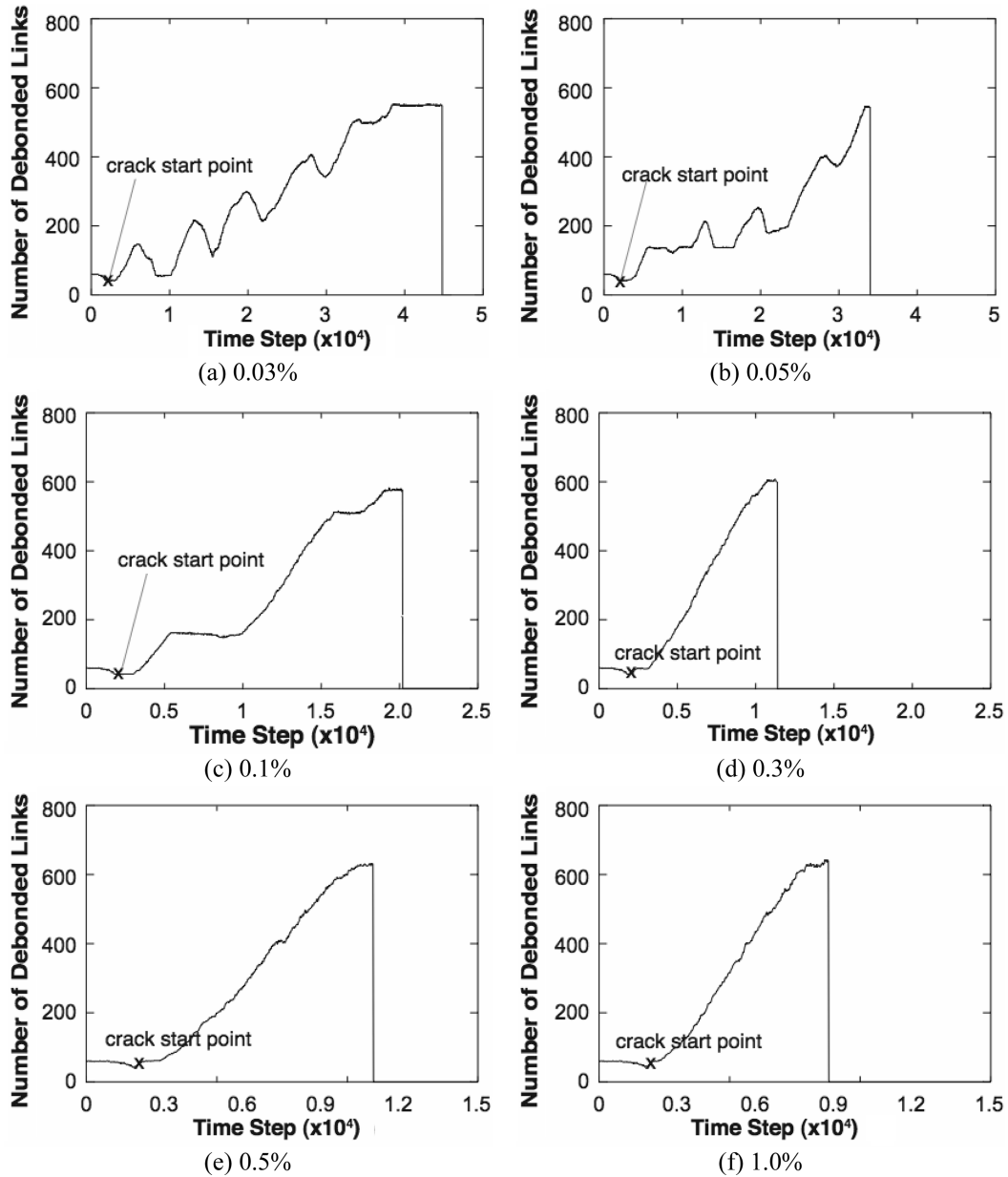(c) 0.1%

(d) 0.3%

(e) 0.5%

(f) 1.0%

Fig. 7 The number of debonded links versus time step relation curves

loading rates. The link is counted as debonded if the distance between two particles is more than the cutoff radius $2r_0$, based on which the crack surface is identified. Note that the time increment Δt in a step is all the same regardless of different loading rates, thus the number of time step is in a fraction of real time unit. In each loading-rate case, the number decreases first in approximately 2000 time steps, which means the initial notch seems to be closed since the wave motion appears from the boundary clamps at the early stage of the simulation. That is to say, the notch needs time to feel the external loading with the wave motion. As can be seen in Figs. 7(a) and (b), the curves fluctuate during the analyses at lower loading rates, which means that the crack surfaces adhere due to the stress wave and inter-particle attraction and then break again, the so-called crack surface interaction. The crack surface interaction cannot occur in the macro-level simulations, and still remains as a mysterious phenomenon in the microscopic behaviors (Fineberg and Marder 1999).
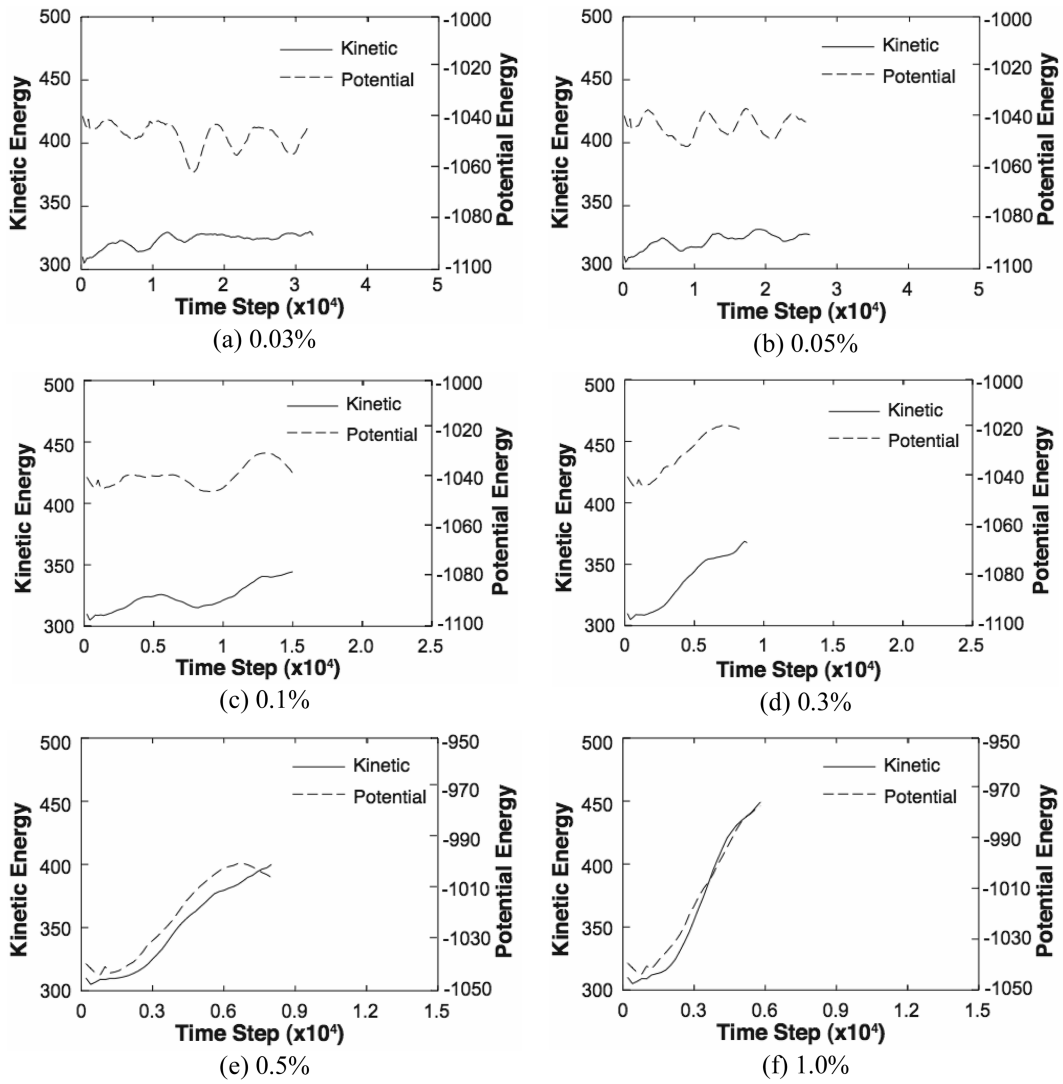

Fig. 8 The kinetic and potential energies versus time step relation curves

The curves in Figs. 7(b) and (c) have plateaus that appear sporadically during the crack growth, which denotes the crack stops under a certain condition, called crack arrest (Bergkvist 1974). The case 0.05% (Fig. 7(b)) shows both the fluctuation and the plateauin the curve, so it can be considered as an intermediate stage. Crack surface interaction/crack arrest is due to the insufficiency of energy inflow into the system. A crack grows when the energy is concentrated at the crack tip such that it is sufficient to break the linkage of particles, but the energy inflow rate cannot keep in pace with the crack propagation speed in lower loading-rate cases. Contrastively, in cases faster than 0.3% of v_s, the crack propagates freely and the crack grows to the complete separation of the specimen in shorter time as the loading rate increases (Figs. 7(d), (e), and (f)). These features might be confused with statements about Fig. 4, where it is said that the crack propagation is retarded as the loading rate increases, but that was the global strain-based comparison, not the time-based one.

For better understanding of the failure mechanism through the energy concept approach, the energy variations with the time step are plotted in Fig. 8. The kinetic and potential energies are calculated around the crack tip. As the crack moves, by tracking the crack tip to be placed on the center of a particular window of $200r_0$ by $200r_0$, the total kinetic and potential energies of the particles inside the window are calculated, respectively. In lower loading-rate cases, the curves show fluctuations in part but little energy changes over all (Figs. 8(a) and (b)). In the cases of the loading rate over 0.3% of v_s, both the energies increase during the cracking process (Figs. 8(d), (e), and (f)). Since the kinetic energy can be expressed in a fraction of temperature, the increase of kinetic energy indicates the heat generation around the crack tip. Also, the increase of potential energy can result in the accumulation of the strain energy in that particular region. From the results, we can infer that the energy inflicted
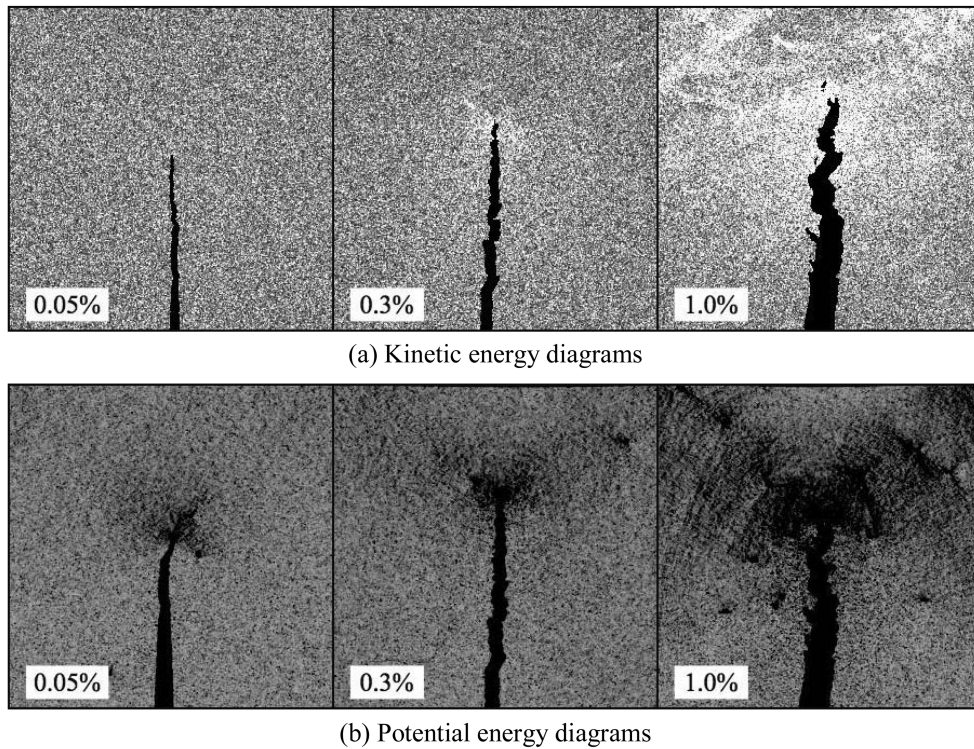

(a) Kinetic energy diagrams

(b) Potential energy diagrams

Fig. 9 Energy variation snapshots around the crack tip (0.05%, 0.3%, and 1.0% of v_s)

by the external loading is entirely used up to generate the new crack surface at lower loading rates. At higher loading rates, however, the inflow of the energy exceeds that required for fracture formation and the extra energy may be accumulated with other forms of energy in the system.

Fig. 9 shows the snapshots of the kinetic and potential energy diagrams for the cases of 0.05%, 0.3%, and 1.0% of v_s. The range of the projected diagram is $200r_0$ by $200r_0$ around the crack tip, similar to how the total kinetic and potential energy variations are calculated for the particular window. As shown in Fig. 9(a), the bright region appears more spaciously in the case at 1.0% of v_s, which indicates that the particles have higher kinetic energy around the crack tip. From this appearance, the description of the heat generation around the crack tip is corroborated visually. In Fig. 9(b), the higher potential zone, where the dark spots appear, outspreads from the crack tip in the case of higher loading rates, as mentioned about the lower density zone above. For the LJ potential function, the potential energy increases as particles become more distant under the tensile loading conditions. Thus, the higher potential zone can represent the plastic zone, similar to the lower density zone. Besides, the plastic zone has been observed to be butterfly shaped in usual experimental works (Buehler and Gao 2006), and the dark region takes after that shape.

5. Conclusions

In this paper, the numerical experiments of the direct tensile test are performed and the results are presented. The results strongly suggest that the dynamic fracture behavior of a LJ potential-based material at high loading rates might vary significantly when compared with the static loading cases. The main rate dependent features observed as the loading rate increases are:
- The crack growth seems to be retarded in the strain-based comparison.
- However, the actual crack propagation speed is higher.
- The area of plastic zone is enlarged and activated toward the direction of the crack growth.
- Voids nucleated during the cracking process can induce multiple crack fronts and crack branching.
- Crack surface becomes rougher and the crack surface length increases.
- The shockwave generated form the crack tip propagates through the specimen more intensively.
- The crack shows the incisive propagation without crack surface interaction/crack arrest.
- Local heat generation appears around the crack tip.

From the observations, the dynamic features and rate dependent characteristics are mainly interpreted by the energy inflow and consumption rates in unit time. The excessive energy inflow into the specimen causes unstable behaviors such as void nucleation, multiple crack fronts, crack branching, and change of the crack growth direction, although the crack propagation in strain-based comparison appears to be retarded due to the insufficiency of time for crack propagation. As mentioned in the Introduction, the crack speed is limited to the Rayleigh wave speed (Freund 1998), in other words, the system has a limited energy consumption rate for the cracking process. Thus, the crack can hardly move in a relatively short time with extremely high loading rates. On the contrary, the lack of energy inflow induces crack surface interaction/crack arrest during the crack propagation, which can only appear at a microscopic level. Instead, the system uses the energy only for further crack formation and the formation becomes composed in time, so the crack grows in a clean and smooth path and the brittle failure features are observed in strain-based comparison.

Although the results show many rate dependent features in dynamic fracture mechanics, this study

gives only qualitative insights about the failure mechanism. Thus, future researches should be reserved for quantifying the material properties for application to practical engineering fields from the qualitative characteristics obtained in this study.

References

Abraham, F.F. (2001a), "Crack dynamics in brittle fracture: An atomistic study", *Nuclear Instruments and Methods in Physics Research B*, **180**, 72-76.

Abraham, F.F. (2001b), "The atomic dynamics of fracture", *J. Mech. Phys. Solids*, **49**, 2095-2111.

Anderson, T.L. (1995), *Fracture Mechanics 3rd Edition*, CRC Press, Inc., Florida.

Bergkvist, H. (1974), "Some experiments on crack motion and arrest in polymethyl-methacrylate", *Eng. Fract. Mech.*, **6**, 621-626.

Broberg, K.B. (1979), *On the Behaviour of the Process Region at a Fast Running Crack Tip*, Springer.

Buehler, M.J., Abraham, F.F. and Gao, H. (2003), "Hyperelasticity governs dynamic fracture at a critical length scale", *Nature,* **426**(13), 141-146.

Buehler, M.J. and Gao, H. (2006), "Dynamical fracture instabilities due to local hyperelasticity at crack tips", *Nature,* **439**, 307-310.

Döll, W. (1973), "An experimental study of the heat generated in the plastic region of a running crack in different polymeric materials", *Eng. Fract. Mech.*, **5**, 259-268.

Eshelby, J.D. (1971), "Fracture mechanics", *Science Progress*, **59**(234), 161-179.

Fineberg, J. and Marder, M. (1999), "Instability in dynamic fracture", *Phys. Rep.*, **313**, 1-108.

Freund, L.B. (1998), *Dynamic Fracture Mechanics*, Cambridge University Press.

Gao, H., Huang, Y. and Abraham, F.F. (2001), "Continuum and atomistic studies of intersonic crack propagation", *J. Mech. Phys. Solids,* **49**, 2113-2132.

John, R. and Shah, S. (1990), "Mixed-mode fracture of concrete subjected to impact loading", *J. Struct. Eng.,* **116**(3), 585-602.

Kobayashi, A., Ohtani, N. and Sato, T. (1974), "Phenomenological aspects of viscoelastic crack propagation", *J. Appl. Polym. Sci.*, **18**, 1625-1638.

Kozhushko, A.A. and Sinani, A.B. (2005), "Loading velocity and brittleness of solids", *Physics of the Solid State*, **47**(5), 836-839.

Krivtsov, A.M. (2003), "Molecular dynamics simulation of impact fracture in polycrystalline materials", *Meccanica*, **38**, 61-70.

Krivtsov, A.M. and Wiercigroch, M. (2001), "Molecular dynamics simulation of mechanical properties for polycrystal materials", *Mater. Phys. Mech.,* **3**, 45-51.

Lok, T.S., Zhao, P.J. and Lu, G. (2003), "Using the split Hopkinson pressure bar to investigate the dynamic behaviour of SFRC", *Magazine of Concrete Research,* **55**(2), 183-191.

Ravi-Chandar, K. and Knauss, W.G. (1984), "An experimental investigation into dynamic fracture: II. Microstructural aspects", *Int. J. Fract.*, **26**, 65-80.

Robertson, D.H., Barrett, J.J.C., Elert, M.L. and White, C.T. (1997), "Self-similar behavior from molecular dynamics simulations of detonations", *Proceedings of the 10th American Physical Society Topical Conference on Shock Compression of Condensed Matter*, Amherst, Massachusetts, July-August.

Wagner, N.J., Holian, B.L. and Voter, A.F. (1992), "Molecular-dynamics simulation of two-dimensional materials at high strain rates", *Phys. Rev. A,* **45**(12), 8457-8470.

Zhou, S.J., Beazley, D.M., Lomdahl, P.S. and Holian, B.L. (1997), "Large-scale molecular dynamics simulations of three-dimensional ductile failure", *Phys. Rev. Lett.,* **78**(3), 479-482.

Zhou, S.J., Lomdahl, P.S., Thomson, R. and Holian, B.L. (1996), "Dynamic crack processes via molecular dynamics", *Phys. Rev. Lett.,* **76**(13), 2318-2321.

Zimmerman, C., Klemm, W. and Schonert, K. (1984), "Dynamic energy release rate and fracture heat in polymethylmethacrylate(PMMA) and a high strength steel", *Eng. Fract. Mech.*, **20**, 777-782.